# Molecular determinants of cadherin ideal bond formation: Conformation-dependent unbinding on a multidimensional landscape

Kristine Manibog[a,b], Kannan Sankar[c,d], Sun-Ae Kim[a,b], Yunxiang Zhang[e], Robert L. Jernigan[a,c,d,f], and Sanjeevi Sivasankar[a,b,1]

[a]Department of Physics and Astronomy, Iowa State University, Ames, IA 50011; [b]Ames Laboratory, US Department of Energy, Ames, IA 50011; [c]Bioinformatics and Computational Biology Interdepartmental Program, Iowa State University, Ames, IA 50011; [d]Roy J. Carver Department of Biochemistry, Biophysics and Molecular Biology, Iowa State University, Ames, IA 50011; [e]Department of Molecular and Cellular Physiology, Stanford University, Stanford, CA 94305; and [f]L. H. Baker Center for Bioinformatics and Computational Biology, Iowa State University, Ames, IA 50011

Edited by Barry Honig, Howard Hughes Medical Institute, Columbia University, New York, NY, and approved July 19, 2016 (received for review March 10, 2016)

**Classical cadherin cell–cell adhesion proteins are essential for the formation and maintenance of tissue structures; their primary function is to physically couple neighboring cells and withstand mechanical force. Cadherins from opposing cells bind in two distinct *trans* conformations: strand-swap dimers and X-dimers. As cadherins convert between these conformations, they form ideal bonds (i.e., adhesive interactions that are insensitive to force). However, the biophysical mechanism for ideal bond formation is unknown. Here, we integrate single-molecule force measurements with coarse-grained and atomistic simulations to resolve the mechanistic basis for cadherin ideal bond formation. Using simulations, we predict the energy landscape for cadherin adhesion, the transition pathways for interconversion between X-dimers and strand-swap dimers, and the cadherin structures that form ideal bonds. Based on these predictions, we engineer cadherin mutants that promote or inhibit ideal bond formation and measure their force-dependent kinetics using single-molecule force-clamp measurements with an atomic force microscope. Our data establish that cadherins adopt an intermediate conformation as they shuttle between X-dimers and strand-swap dimers; pulling on this conformation induces a torsional motion perpendicular to the pulling direction that unbinds the proteins and forms force-independent ideal bonds. Torsional motion is blocked when cadherins associate laterally in a *cis* orientation, suggesting that ideal bonds may play a role in mechanically regulating cadherin clustering on cell surfaces.**

single-molecule biophysics | mechanobiology | simulations | AFM | cell adhesion

The formation and maintenance of multicellular structures rely upon specific and robust intercellular adhesion (1). Cell–cell adhesion proteins, such as classical cadherins, are crucial in these processes (2–4). Cadherins are $Ca^{2+}$-dependent transmembrane proteins that mediate the integrity of all soft tissues. One of their principal functions is to bind cells and dampen mechanical perturbations; however, the biophysical mechanism by which cadherins tune adhesion is not understood. Here, we combine predictive simulations with quantitative single-molecule force-clamp measurements to show that E-cadherin (Ecad), a prototypical classical cadherin, dampens the effect of tugging forces by switching conformations and unbinding along a strongly preferred pathway on a multidimensional landscape.

Cadherin adhesive function resides in their ectodomain that is comprised of five extracellular (EC) domains arranged in tandem (5–9). Structural studies (10–15) and single-molecule fluorescence measurements (16) show that opposing ectodomains bind in two distinct *trans* conformations: strand-swap dimers (S-dimers) and X-dimers. S-dimers, which have a higher binding affinity, are formed by the exchange of a conserved tryptophan at position 2 (W2) between binding partners (10, 13, 17–19). In contrast, low-affinity X-dimers are formed by extensive surface interactions around the linker region that connects the two outermost domains (EC1–EC2) (11, 12, 14–17). In the absence of force, X-dimers are believed to serve as a kinetic intermediate in S-dimer formation (12, 16, 20) and dissociation (19). NMR studies show that *trans* dimer formation is a slow process that occurs over a ∼1-s timescale (20); this slow dimerization process presumably enables cadherins to sample metastable, intermediate conformations along their reaction coordinate. Furthermore, double electron–electron resonance (DEER) experiments (21) showed that classical cadherins exist in an equilibrium ensemble of multiple conformational states and that the dynamic exchange between conformations has important effects on cell–cell adhesion. However, the pathway by which cadherins interconvert between X-dimers and S-dimers and its effect on adhesion is not well understood.

Using single-molecule force-clamp experiments with an atomic force microscope (AFM) coupled with atomistic computer simulations, we recently showed that X-dimers and S-dimers have distinctly different mechanical properties (22, 23). Whereas cadherin mutants trapped in an X-dimer conformation formed catch-slip bonds (i.e., molecular interactions that become longer-lived when pulled), mutants trapped in an S-dimer conformation formed slip bonds with lifetimes that decrease upon application of increasing

## Significance

Multicellular assemblies rely on the robust binding of classical cadherin cell–cell adhesion proteins to maintain their integrity and withstand mechanical stress. Cadherins can form adhesive interactions that are insensitive to tugging forces; however, the biophysical mechanism for cadherin force insensitivity is unknown. Here, we integrate single-molecule biophysical measurements with computer simulations to show that cadherins, which are known to bind in two distinct conformations, adopt an intermediate structure as they transition between their alternate conformations. When this intermediate structure is pulled, it unbinds along a force-independent pathway that makes it insensitive to tugging forces. Force-independent unbinding is blocked when cadherins associate laterally, suggesting a physical mechanism by which mechanical force enhances cadherin clustering on the cell surface.

Author contributions: S.S. designed research; K.M., K.S., and S.-A.K. performed research; Y.Z. contributed new reagents/analytic tools; K.M., K.S., R.L.J., and S.S. analyzed data; and K.M., K.S., R.L.J., and S.S. wrote the paper.

The authors declare no conflict of interest.

This article is a PNAS Direct Submission.

[1]To whom correspondence should be addressed. Email: sivasank@iastate.edu.

This article contains supporting information online at www.pnas.org/lookup/suppl/doi:10.1073/pnas.1604012113/-/DCSupplemental.

tensile force. In contrast, wild type (WT) cadherins formed interactions that were insensitive to pulling force (i.e., ideal bonds) (22). We hypothesized that WT cadherins formed ideal bonds because they adopt an intermediate conformation that unbinds along a coordinate that is perpendicular to the pulling force; this intermediate conformation is formed when WT cadherins transition between X-dimers and S-dimers. However, the structure of this intermediate conformation and the mechanistic consequences of its formation and rupture are unknown. Here, we combine atomistic and coarse-grained simulations with quantitative single-molecule force-clamp measurements to resolve these questions.

We first build the energy landscape for Ecad *trans* dimers and investigate the transition pathway for the interconversion between X-dimers and S-dimers by evaluating the principal motions (24, 25) of cadherin experimental structures using principal component analysis (PCA). Construction of the multidimensional energy landscape of cadherins sheds light on the different conformations of Ecad dimers and the steric constraints that govern their interconversion. Next, with all-atom molecular dynamics (MD) simulations and PCA, we examine the conformational evolution of different cadherin structures and identify key elements crucial to their interconversion. By using steered MD (SMD) simulations, we investigate the force-induced unbinding dynamics of different cadherin structures and predict the conditions under which ideal bonds are observed. Finally, we experimentally test these predictions by generating mutants that either inhibit ideal bond formation by trapping Ecad in an S-dimer conformation (K14E) or promote ideal bond formation by enhancing the sampling of the intermediate state (W2F). We use single-molecule AFM force-clamp measurements to measure the force-dependent lifetimes of WT-Ecad, the K14E mutant, and the W2F mutant.

Our results show that as Ecads shuttle between X-dimer and S-dimer conformations they sample an intermediate state; encouragingly, both coarse-grained and all-atom simulations suggest similar transition pathways between S-dimers and X-dimers. When this intermediate conformation is pulled, it undergoes a torsional motion perpendicular to the pulling direction, which results in unbinding that is insensitive to force. Because this torsional motion is blocked when cadherins associate laterally on the cell surface in a *cis* orientation, our studies suggest that only *trans* dimers that are not incorporated into *cis* clusters can form ideal bonds. Given the exceedingly short lifetimes of ideal bonds, it is likely that mechanical force preferentially ruptures standalone *trans* dimers and enhances the concentration of cadherin clusters in intercellular junctions.

## Results

**Cadherin Energy Landscape and Transition Pathway for the Interconversion Between X-Dimers and S-Dimers.** To determine the classical cadherin energy landscape, we used PCA to evaluate the most important coordinate variations (24, 25) from a set of 11 classical cadherin dimeric crystal structures that include both X-dimers and S-dimers. The entire structural variation present in the set could be summarized in only a few important motions or principal components (PCs), which provided the directions of fluctuation of each residue along the x, y, and z coordinates. Several studies have shown that such variations extracted from sets of experimental structures closely correspond to motions sampled from a single structure using MD simulations or coarse-grained elastic network models (ENMs) (26, 27) and usually correspond to functionally important conformational changes of the protein (28). Whereas the first principal motion (represented by PC1) corresponded to a scissoring motion between the interacting protomers, the second principal motion (represented by PC2) corresponded to a twisting motion of the two monomers with respect to the each other along a plane perpendicular to PC1 (Fig. 1). These two principal motions, PC1 and PC2, captured 94% and 5%, respectively, of the total variation in the dataset, suggesting that these two motions are highly effective in describing all of the motions present within the set of classical cadherin crystal structures.

Because these are the most important directions of structural variations, the two PCs represent a convenient and efficient set of coordinates upon which to construct energy landscapes (29, 30). Analogous to the x, y, and z directions, the PC directions are orthogonal and can be considered to form a multidimensional landscape, and the structures can be projected onto this space. The energy landscape of cadherin along the PC1 and PC2 coordinates was constructed as described in *Methods* (Fig. 1*A*). Structures were sampled along PC1 and PC2 by deforming a representative structure (by linearly extrapolating its 3D coordinates) along each PC direction as described in ref. 31. Then, the energy of each structure on this landscape was estimated using coarse-grained knowledge-based potentials. We used coarse-grained models in this case because the conformational changes in cadherins involve remarkably large motions between the protomers (changes of order of nanometers). Previous works have shown that, for large conformational changes, physics-based all-atom fields are not as good at discriminating native structures of proteins from decoy models as are knowledge-based potential functions based on frequencies of contacts between different types of amino acids, counted in a large nonredundant set of (>500) known crystal structures of diverse proteins (32–34). We specifically used an optimized potential function combining long-range four-body contacts, which are appropriate for densely packed proteins, together with short-range terms, which have been shown to perform well in discriminating between native and nonnative modeled structures

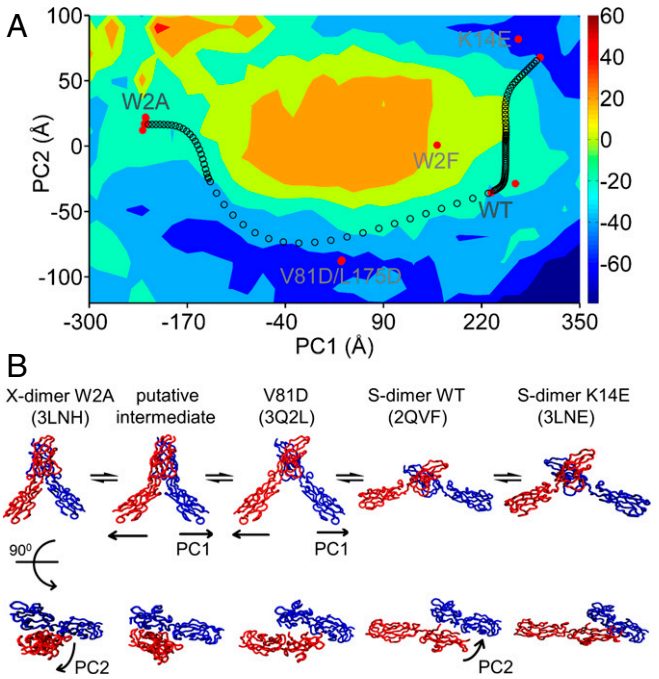


**Fig. 1.** Energy landscape and transition state pathway of Ecad dimers. (*A*) Two-dimensional energy landscape of Ecad constructed along PC1 and PC2 extracted from a set of 11 crystal structures (solid red circles) are shown as a contour plot in VIBGYOR color format (violet = low energies and red = high energies). X-dimer structures are located at low values of PC1 (left), and S-dimers are at high values of PC1 (right). The intermediate structures along the transition paths between different forms as obtained by using the PATH-ENM server are shown as open black circles. (*B*) Visualization of the transition between X-dimers and S-dimers shows the computed intermediates along the transition path between the two forms. The X-dimer first twists along PC2 to give rise to an intermediate, which moves along PC1 to give rise to the WT, which then twists back in the PC2 direction to yield the S-dimer K14E structure.

(35). Following this, the energies of structures on the entire landscape were visualized in the form of an energy contour plot and the experimental structures were shown as solid red circles (Fig. 1*A*). It is worth noting that the 11 experimental structures were observed to lie in low-energy regions of the energy landscape; structures along low values of PC1 corresponded to X-dimers, whereas the structures along high values of PC1 corresponded to S-dimers. Two clusters of S-dimers were observed, corresponding to low and high values of PC2, indicating structures that differ in their twist angles (Fig. 1*A*). Without sufficient twist of the monomers relative to one another (along PC2), the scissoring motion (along PC1) caused the EC domains to overlap with each other. Consequently, this resulted in a high-energy region in the center of the landscape where no crystal structures were observed (Fig. 1*A*). One point to note is that the energy landscape does not reflect the free energy of dimer formation from monomers, but simply captures the relative energies of various dimeric conformations.

To understand how the intrinsic fluctuations of the structures drive the conformational change between X-dimers and S-dimers, we derived the transition paths between W2A mutant and WT forms as well as between the WT and K14E mutant forms by using a coarse-grained ENM-based interpolation, performed by using the PATH-ENM server (36). The transition intermediates between the two conformations were projected onto the PC1–PC2 space as shown in Fig. 1*A*. Interestingly, the transition path between the W2A mutant [Protein Data Bank (PDB) ID code 1EDH] exhibiting an X-dimer structure and WT S-dimer crystal structure (PDB ID code 2QVF) passed close to the crystal structures 3Q2L and 3Q2N (V81D and L175D *cis* dimer mutants forming S-dimers). The conformational change between the WT and the K14E mutant (PDB ID code 3LNI) primarily involved motion along PC2, reiterating the fact that the K14E mutant adopted a slightly different twist angle.

The transition path between the X-dimer and the S-dimer visualized on these structures is shown in Fig. 1*B*. Starting from the X-dimer (PDB ID code 3LNH), the EC1–2 domains twisted away from one another along PC2 to form an intermediate shown in the second position in Fig. 1*B*, before reaching the third position, by moving along PC1 corresponding to the experimental structure (PDB ID code 3Q2L). A further sliding along PC1 (increasing the angle between the two molecules) formed the WT conformation (PDB ID code 2QVF). This structure then twisted back along PC2 to reach the K14E S-dimer (PDB ID code 3LNE). The X-dimer could not slide directly along the PC1 direction because the EC1–EC2 domains clashed on such a path.

**WT and Conformational-Shuttling Mutants Form a Metastable, Intermediate Dimer State.** Next, we used MD simulations to investigate the molecular determinants of cadherin conformational interconversion. Since only the EC1–EC2 domains are involved in *trans* binding, we used four EC1–EC2 *trans* dimer crystal structures in our simulations: (*i*) WT cadherin (PDB ID code 2QVF), (*ii*) mutant W2A (PDB ID code 3LNH), which replaces the swapped Trp with an Ala and traps cadherin in an X-dimer conformation (12), (*iii*) mutant K14E (PDB ID code 3LNE), which eliminates a key salt bridge in the X-dimer interface and traps cadherin in an S-dimer structure (12), and (*iv*) W2F, "conformational-shuttling" mutant (PDB ID code 4NUQ), which relieves the strain in the swapped N-terminal β-strand and forms weak binding affinity S-dimers (37); previous DEER experiments showed that this W2F mutant construct populates an equilibrium ensemble of X-dimers and S-dimers (21). All structures used in these simulations were from Ecad except the W2F mutant, which was from N-cadherin (Ncad), a closely related type I classical cadherin that shares a high sequence identity (~77%) of its N-terminal β-strand with Ecad (~53% sequence identity over the whole EC1–EC2 dimer structure), with conserved amino acids forming the swapping interface. Because cadherin dimerization is a rather slow process that is completed in ~1 s, we performed long-duration 150-ns MD simulations (Fig. 2 and Movies S1–S4) to capture conformational interconversion in these structures. All MD simulations executed on W2A, W2F, WT, and K14E dimer structures (Fig. 2 *A*, *D*, *G*, and *J*) were performed using GROMACS with a GROMOS 53a6 all-atom force field (38, 39) with 2-fs integration time steps.

Although the design rules for cadherin strand swapping have been extensively studied (37), the process by which dimers interconvert between different structural conformations have not been investigated. Since X-dimers are believed to serve as the first intermediate along the pathway to strand swapping (12, 16, 20), we assessed how the dimer structures evolved over time by measuring the root-mean-square displacement (RMSD) of every simulation frame relative to both the X-dimer crystal structure and to the structure at the start of the simulation (Fig. 2 *B*, *E*, *H*, and *K*). We also analyzed the principal motions of the dimer structures by projecting the MD trajectories onto the PC1–PC2 space of cadherin dimer crystal structures (Fig. 2 *C*, *F*, *I*, and *L*). Our data showed that W2A mutant X-dimers stabilized rapidly and maintained a relatively low RMSD of 0.38 nm while remaining in their original conformation (Fig. 2 *A* and *B*). Moreover, this mutant was able to sample only a small space along PC1–PC2, with standard deviations (SDs) of 1.8 nm and 4.4 nm, respectively (Fig. 2*C*), which suggested strong resistance to conformational change.

In contrast, both the W2F and WT dimer structures seemed to convert from an S-dimer structure at the start of the simulation to an X-dimer–like conformation, albeit with the swapped amino acids still within their complementary hydrophobic pockets (Fig. 2 *D*–*I*). The RMSD of W2F and WT dimers relative to the W2A crystal structure decreased from initial values of 2.1 nm and 2.4 nm, respectively, to 1.1 nm when the structures converged. Simultaneously, the RMSDs of W2F and WT dimers relative to their initial structures increased to 1.8 nm and 1.7 nm, respectively (Fig. 2 *E* and *H*). Furthermore, the PCs of both the W2F mutant and WT Ecad approached the low PC1 values of the X-dimer, with measured PC1 SDs of 7.7 nm and 10.3 nm, respectively, and PC2 SDs of 6.9 nm and 5.5 nm, respectively (Fig. 2 *F* and *I* and Table S1). Finally, whereas the low-affinity W2F mutant reached an X-dimer–like conformation within ~30 ns, the higher-affinity WT Ecad required ~75 ns to adopt a similar structure (Fig. 2 *E* and *H*). The more rapid equilibration of W2F mutant dimers and comparable SDs of the W2F mutant both along PC1 and PC2 directions is consistent with Phe2 being smaller than Trp2, which provides a weaker constraint in the PC1–PC2 space, allowing the W2F mutant to shuttle more readily between S-dimer and X-dimer and adopt an X-dimer–like structure (37) (Fig. 2*D*). Nonetheless, although we performed 150-ns MD simulations for both WT and W2F cadherin dimers, these structures (Fig. 2 *D* and *G*) never reached the X-dimer conformation (Fig. 2*A*). This is likely due to the huge disparity in timescales between our MD simulations and experimentally measured (20) structural conversion. Consequently, the final MD structure of W2F (Fig. 2*D*) and WT (Fig. 2*G*) dimers correspond to an "intermediate" state in the interconversion between S-dimers and X-dimers. Our RMSD result, which shows that the WT dimer adopts a structure different from its starting conformation, is consistent with previous MD simulations, albeit with a different force field and significantly shorter production runs (40).

Similar to the W2A mutant, the K14E mutation abolished the ability of Ecad to shuttle between multiple conformations. Whereas the K14E mutants attempted to adopt an X-dimer conformation, as indicated by the spike in RMSD observed at ~12 ns, the repulsive interactions introduced by mutating K14 to E14 kept this mutant from forming an X-dimer structure (Fig. 2*J*). Consequently, these dimers remained in a strand-swap conformation

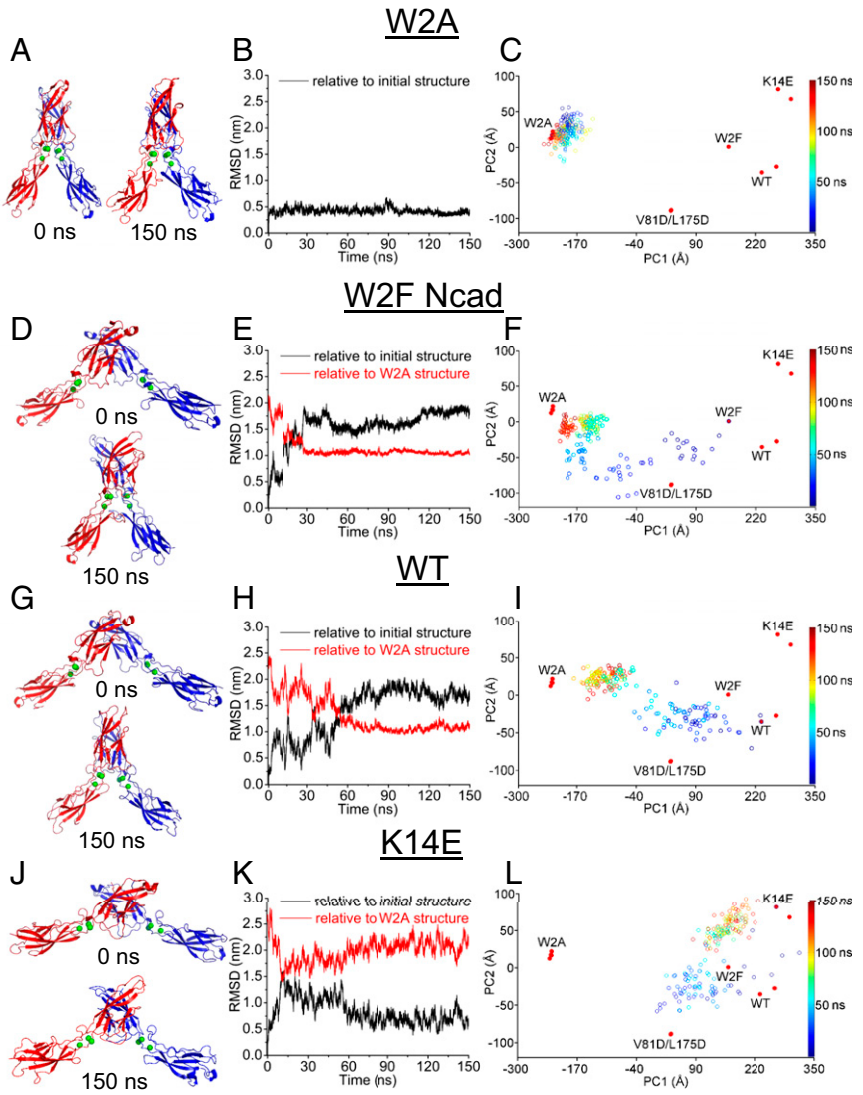


**Fig. 2.** WT cadherin and conformational-shuttling mutant form an intermediate dimer state. Formation of the intermediate state was investigated using 150-ns MD simulations on four EC1-EC2 *trans* dimer crystal structures: W2A Ecad mutant, W2F Ncad mutant, WT-Ecad, and K14E Ecad mutant. Conformational changes in the dimer structures were monitored by measuring the RMSD of each simulation frame relative to both the X-dimer crystal structure and the structure at the start of the simulation. PCA was used to calculate the principal motions by projecting structures along the MD trajectories onto the PC1–PC2 space obtained from dimer crystal structures (PC1 and PC2 are parallel and perpendicular to the plane of the page). Snapshots at 0 ns and 150 ns serve as visual guides for the change in the dimer structures. Green spheres are $Ca^{2+}$ ions. (*A*) Snapshots of W2A structures at 0 ns and 150 ns are similar, showing that they remain in an X-dimer conformation (*B*) with relatively small, fairly constant RMSD of 0.38 nm relative to its initial structure. (*C*) The observed W2A PC scores are tightly clustered near the initial structure with an SD of 1.5 nm and 3.9 nm, along PC1 and PC2 directions, respectively. In contrast, (*D*) snapshots of the W2F mutant at 0 ns and 150 ns show that the W2F S-dimer structure shuttles toward an X-dimer conformation. This is evident from (*E*) its RMSD relative to its initial structure, which increases to a stable average value of 1.84 nm whereas the RMSD relative to the W2A crystal structure decreases to an average value of 1.06 nm. Furthermore, (*F*) PC scores approach the X-dimer structure with a significant PC1 SD of 7.7 nm. Similarly, (*G*) WT-Ecad snapshots at 0 ns and 150 ns reveal that the initial S-dimer structure converts to an X-dimer–like conformation (*H*) with measured RMSDs of 1.74 nm and 1.06 nm, relative to its initial structure and W2A crystal structure, respectively. (*I*) PCA on the MD trajectories also shows that the WT structure evolves to an X-dimer–like conformation. (*J*) Snapshots of the K14E mutant at 0 ns and 150 ns clearly show that K14E dimers remain in a strand-swap conformation exhibiting (*K*) relatively low and high RMSD values relative to its initial and W2A crystal structures, respectively. (*L*) In the PC1–PC2 space, its trajectories cluster around the strand-swap conformational structures.

with RMSDs of 0.70 nm and 2.0 nm relative to its initial structure and the X-dimer crystal structure, respectively (Fig. 2*K*). However, as indicated by a PC1 SD of 5.1 nm (Fig. 2*L* and Table S1), the K14E mutant sampled a much larger conformational space compared with W2A X-dimers (Fig. 2*C* and Table S1), although this space was limited only to S-dimer conformations.

This conformational evolution of cadherin structures was also confirmed when we compared the solvent-accessible surface area (SASA) in the MD simulations (Fig. S1). Whereas the SASA of the W2A mutant remained fairly constant throughout the simulation (Fig. S1*A*), suggesting that it remained as an X-dimer, the SASA decreased in the W2F mutant and WT cadherin, which converted from an S-dimer to X-dimer-like conformation (Fig. S1 *B* and *C*). In contrast, SASA measurements in K14E remained relatively constant with the highest observed value (Fig. S1*D*). Aside from the measured SASA, the final K14E conformation resembled its original structure with an angle of 77° between opposing EC1 domains; this angle was much wider compared with angles of 29°, 45°, and 21° for the final WT, W2F, and W2A structures, respectively (Table S2).

**Conformational Interconversion Depends on the K14–D138 Salt-Bridge Interaction.** Since one of the principal interactions in an X-dimer is the salt bridge formed between K14 on the EC1 domain of one protomer and D138 at the apex of the EC2 domain of its opposing partner, we monitored the distance between these amino acids in the MD simulations of the W2A mutant, the W2F mutant, WT cadherin, and the K14E mutant dimer structures. Our data showed that in the W2A mutant the K14–D138 salt bridge pair "clipped" the cadherins together into an X-shaped conformation, such that it reduced any observable dynamic motion along PC1 and PC2 while maintaining its original conformation throughout the 150-ns MD simulation (Fig. 3*A*). Consequently, that distance between the center of mass of the K14 and D138 amino acids in the X-dimer remained fairly constant at ∼0.92 nm (Fig. 3 *B* and *C*). Similarly, as the W2F-Ncad and WT Ecad converted from an S-dimer to an X-dimer–like structure, the R14–D137 pair (W2F-Ncad, Fig. 3 *D*–*F*) and K14–D138 pair (WT Ecad, Fig. 3 *G*–*I*) began to come together, approaching a final distance of 1.25 nm between the center of masses of the amino acid pairs. However, salt bridge formation was not completed within the 150-ns duration of the MD simulation. In contrast, the K14E mutant, where X-dimer formation was abolished due to a repulsive interaction between E14 and D138, showed a large (∼2.7 nm) distance between E14 and D138 (Fig. 3 *J*–*L*).

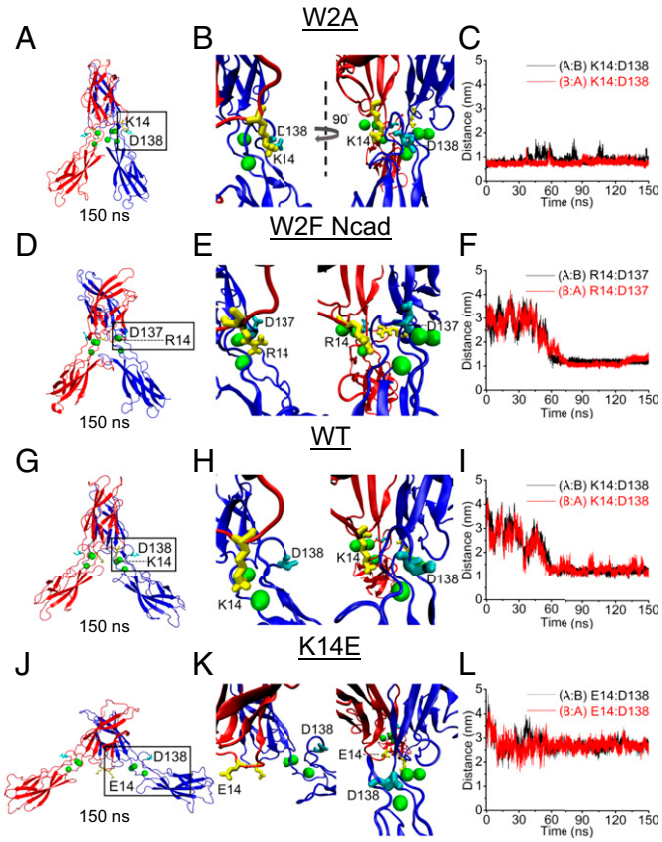


**Fig. 3.** K14–D138 salt-bridge pair locks X-dimers. Center of mass distances between the complementary K14–D138 (R14–D137 in W2F Ncad) salt-bridge pairs were monitored. K14/R14 are shown in yellow and D137/D138 are shown in cyan. Green spheres are $Ca^{2+}$ ions. (*A*–*C*) Distance measured between the center of masses of the K14 and D138 amino acid residues on the two protomers (proteins A and B) remain stable in the W2A X-dimer structure. (*D* and *E*) The W2F Ncad dimer structure has two complementary R14–D137 salt-bridge pairs, which exhibit (*F*) decreasing distance relative to each other during a 150-ns MD run. (*G* and *H*) WT dimer structure also shows (*I*) decreasing distance between K14 and D138. (*J* and *K*) Mutating K14 to E14 prevents the two opposing proteins from coming together due to electrostatic repulsion. As a result, (*L*) the distance between E14 and D138 remains fairly constant at ∼2.7 nm.

**Intermediate Dimer States Exhibit Force-Induced Conformational Motion Perpendicular to the Pulling Direction.** Because cadherins populate an intermediate state as they interconvert between X-dimers and S-dimers, we performed SMD simulations to determine the mechanical properties of the intermediate conformation and compare them to the force-induced unbinding of X-dimers and S-dimers (Fig. 4 and Movies S5–S8). Although SMD simulations have been previously used to uncover the molecular mechanism by which S-dimers and X-dimers form slip and catch-slip bonds, respectively (23, 41), the mechanical properties of intermediate structures have not been investigated. We therefore performed SMD simulations with 0.4 nm/ns constant pulling velocity in explicit solvent on W2A-Ecad, W2F-Ncad, WT-Ecad, and K14E-Ecad EC1–EC2 dimers. To establish reproducibility, three SMD simulations were performed on each cadherin, using the final conformation from the MD simulation at 150 ns (henceforth referred to as 150-SMD), the structure at 140 ns (henceforth referred to as 140-SMD), and the structure at 100 ns (henceforth referred to as 100-SMD) as initial structures. All SMD simulations used a center-of-mass pulling method using a virtual harmonic spring to dissociate the opposing protomers via a C-terminal residue pulling group. Force was applied in a direction parallel to PC1, pulling the proteins away from one another (Movies S5–S8). All four dimer structures separated under the influence of force, as demonstrated by an increase in angle between the dimers (Fig. 4 *A* and *C*–*F*, red line). However, two distinct sets of unbinding motions were measured for the W2A, W2F, and WT structures: a motion in the pulling direction (along PC1) and a torsional motion perpendicular to the applied force (along PC2) (Fig. 4 *B* and *C*–*E*, black line). In contrast, the K14E mutant primarily moved only in the direction of force application (Fig. 4*F*, black line).

Upon pulling the W2A dimer, we measured a peak-to-peak torsion angle change between opposing EC1 domains, along the PC2 direction, of 39° (150-SMD), 48° (140-SMD), and 46° (100-SMD) (Fig. 4*C*, black line); the SD of this torsional motion was 9° averaged over the three SMD simulations. Similarly, when the W2F dimer intermediate state was pulled, a significant torsional motion with a peak-to-peak EC1–EC1 angle of 47° (150-SMD), 25° (140-SMD), and 34° (100-SMD) (Fig. 4*D*, black line) and an SD of 8° averaged across all three SMD simulations was measured. Pulling the WT-Ecad intermediate state also resulted in a motion perpendicular to the pulling force, comparable to both the W2A and W2F mutants: the peak-to-peak angle change between the EC1 domains along PC2 was 40° (150-SMD), 32° (140-SMD), and 30° (100-SMD), with an SD of 8° averaged over the three SMD simulations (Fig. 4*E*, black line).

Although motion orthogonal to the pulling force was observed in the W2A mutant, the X-dimers formed force-induced hydrogen bonds that resulted in a catch-slip bond formation (23). The formation of force-induced hydrogen bonds was facilitated by the K14–D138 salt bridge pair (Fig. 3 *A*–*C*), which locked the proteins together. Consequently, the EC1–EC1 angular separation in the W2A mutant, averaged across all three SMD simulations, was maintained at ∼14° (smallest among the four *trans* dimers) for ∼9 ns, with minimal torsion unbinding motion, before the opposing EC1 domains started to separate (Fig. 4*C*).

In contrast to W2A mutants, both the W2F and WT intermediate dimer structures did not have the R14–D137 (W2F-Ncad) or K14–D138 (WT-Ecad) salt-bridge pairs. Consequently, averaged across all three SMD simulations, they had a larger EC1–EC1

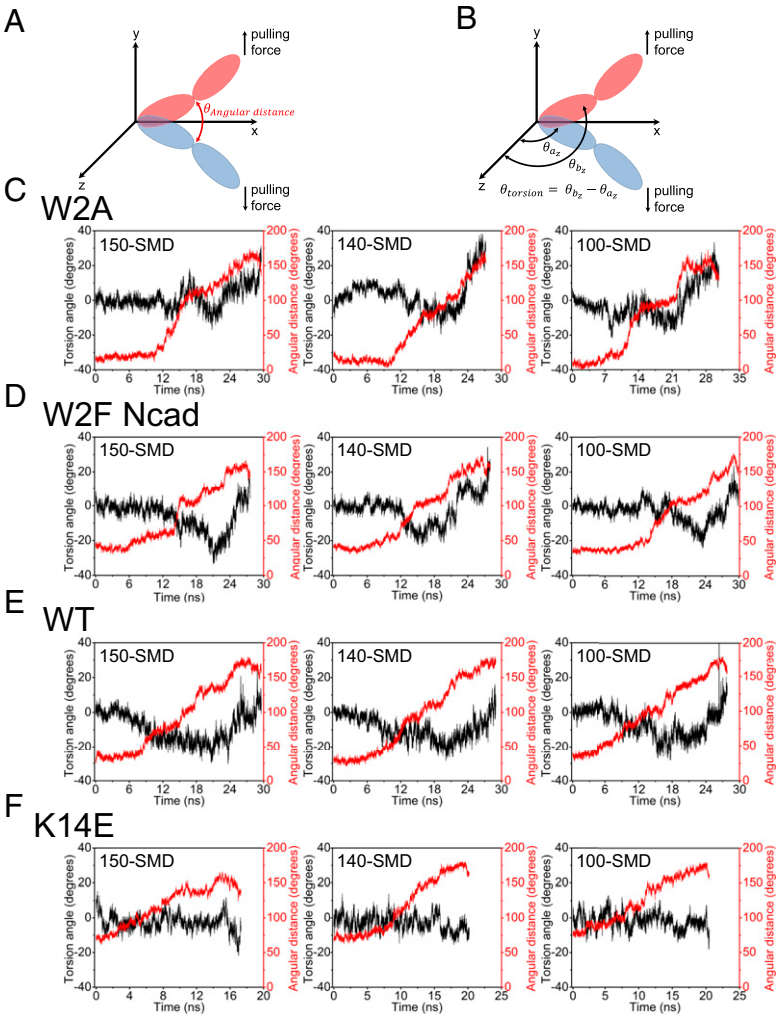


**Fig. 4.** Cadherin intermediate states exhibit unbinding motion perpendicular to the pulling direction. Three SMD simulations were performed on the W2A, W2F, WT, and K14E *trans* dimer structures using the structure at 150 ns (150-SMD), 140 ns (140-SMD) and 100 ns (100-SMD) of the corresponding MD simulation as the starting conformation. When the proteins were pulled apart, we monitored (*A*) their angular separation (depicted by the red arrow) and (*B*) the torsion angle perpendicular to the pulling direction (depicted by the black arrows). The time evolution of the angular separation (red lines) and torsion angle (black lines) show that although the (*C*) W2A mutant, (*D*) W2F intermediate state, and (*E*) WT intermediates state unbind along the pulling direction, they also exhibit significant torsional motion in the orthogonal direction. In contrast, the (*F*) K14E structure unbinds primarily along the pulling direction.

angular separation (~38° in W2F and ~34° in WT) (Fig. 4 *D* and *E*, red line) that increased earlier upon pulling (starting at ~7 ns in W2F and ~5 ns in WT) than for the W2A mutants. However, the evolution of the torsional motion along PC2 was different between the W2F and WT-Ecad dimers. The change in torsional angle between the EC1 domains in the W2F mutant was more abrupt (Fig. 4*D*, black line), likely due to both the smaller Phe2 side chain and fewer interactions at the dimer interface (21, 37). In comparison, the bigger Trp2 indole ring occupied a larger surface area in the hydrophobic pocket of WT-Ecad dimers and was additionally stabilized by a hydrogen bond formed between its side chain NH group and the Asp90 carbonyl group in the hydrophobic pocket (10, 17, 37). This imposed extra constraints on the N-terminal strand and resulted in the slower twisting motion between the opposing EC1 domains in WT-Ecad (Fig. 4*E*, black line). Consequently, the angular separation along PC1 showed a more distinct stepping profile in W2F, where the twisting of the opposing EC1 domains was accompanied by a smaller displacement along PC1 (Fig. 4*D*). Nonetheless, both of these intermediate structures were largely stationary as the two opposing EC1 domains twisted relative to each other, indicating that the dissociation pathway was insensitive to the pulling force (Fig. 4 *D* and *E*, red line). Based on the results of these simulations, we predicted that whereas both W2F mutants and WT-Ecad form force-independent bonds the W2F dimer interactions are more force-insensitive.

Finally, compared with the other cadherin constructs, the K14E mutant had fewer binding interface constraints due to its wide angle (Table S2) and large SASA (Fig. S1*D*). Consequently, pulling the opposing proteins along PC1 posed fewer restrictions on its unbinding motion and the K14E mutant exhibited negligible torsional motion, with an SD of 4° averaged across all three SMD simulations (Fig. 4*F*, black line). Thus, the force-induced dissociation of K14E dimers resulted in a steady unbinding in the PC1 direction with minimal motion along PC2 (Movie S8), suggesting that K14E dimers steadily weaken as force increases, an essential characteristic of a slip bond (22).

**Cadherins Trapped in an Intermediate Dimer State Form Ideal Bonds.** To test the prediction that ideal bonds are formed due to the unbinding from an intermediate state, we performed single-molecule AFM force-clamp spectroscopy measurements using W2F, WT, and K14E Ecad constructs. The complete Ecad ectodomains were

site-specifically biotinylated at a C terminus AviTag sequence and immobilized on PEG-functionalized AFM tips and glass coverslips that had been decorated with streptavidin, a biotin binding protein (16, 22, 42) (Fig. 5*A*). The cadherin functionalized tip and substrate were brought into contact, allowing the proteins to interact for specified contact times (0.3 s or 3.0 s). Subsequently, the tip was pulled away from the surface and clamped at a set force and the survival time for each binding event was measured (Fig. 5*B*). Cadherin binding frequency was adjusted to <5% by controlling the cadherin density on the tip and substrate; Poisson statistics predicted that under these conditions >97% of measured events occur due to the rupture of single X-dimers. Single-molecule fluorescence microscopy experiments have previously shown that under similar experimental conditions a majority of the measured unbinding events occur due to rupture of single *trans* dimers (42). Approximately 1,000–1,500 single-molecule measurements were carried out at five different clamping forces. To directly identify specific binding events and eliminate nonspecific interactions, we simultaneously converted the force-clamp (force vs. time) measurements (Fig. 5*B*) to their corresponding force vs. distance traces and monitored the stretching of the PEG tethers that anchor the interacting cadherins to the AFM tip and substrate (Fig. S2 *A* and *B*) (23). As shown previously (23), this allowed us to unambiguously identify specific single-molecule unbinding events because they occurred at a tip-surface separation corresponding to the stretching of two PEG tethers (Fig. S2*A*). Two methods were then used to determine the bond lifetime at each clamping force (Fig. 5 *C*–*G*). In the first method, bond lifetimes were determined from single-exponential decay fits to the bond survival probability (Fig. 5 *C*–*G*, *Insets* and Fig. S2*C*). In the second method, we computed the weighted mean lifetime at each clamping force without ignoring any outliers. The measured weighted mean lifetimes were in good agreement with the lifetimes obtained from single exponential decay fits (Fig. 5 *C*–*G*). The error bars in the force and lifetime data are the SE of means (SEM) measured using a bootstrap with replacement protocol (43).

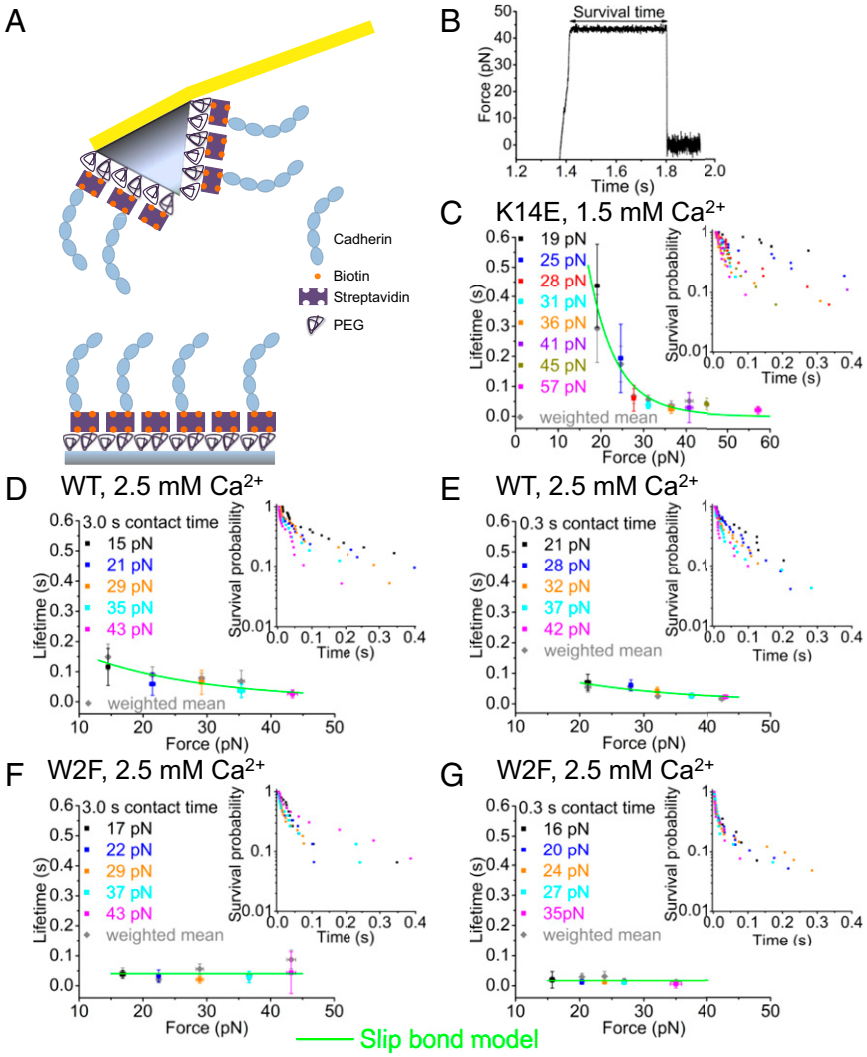


**Fig. 5.** Cadherins trapped in intermediate states form ideal bonds. Single-molecule AFM force-clamp spectroscopy was performed on WT-Ecad, the K14E mutant, and the W2F mutant. (*A*) AFM tips and glass coverslips were functionalized with biotinylated Ecads via a PEG–biotin–streptavidin complex. (*B*) The survival time of each unbinding event was measured as the persistence of the bond at the set force. Two methods were used to determine the bond lifetimes at each clamping force: (*i*) exponential decay fits of the bond survival probabilities and (*ii*) weighted mean lifetimes. (*C*) K14E S-dimers show slip-bond behavior. In contrast, WT-Ecads that interact both for (*D*) 3.0 s and (*E*) 0.3 s show force-independent bonds. W2F mutants show ideal bonds both at (*F*) 3.0-s and (*G*) 0.3-s contact times. All bonds were fitted to the same microscopic slip-bond model (green curve). The survival probabilities of specific unbinding events are shown in the insets of *C*–*G*; for clarity, bond survival probability plots are zoomed in.

We first measured the force-dependent bond-lifetimes of K14E mutants in 1.5 mM $Ca^{2+}$. Our experiments showed that the K14E mutant forms slip bonds, their lifetimes decreased with increasing force (Fig. 5*C*). This slip-bond data are in good agreement with previous results demonstrating that K14E S-dimers form slip bonds in 2.5 mM $Ca^{2+}$ (22) and supports the predictions of our computer simulations showing that K14E mutants are always trapped in an S-dimer conformation and that pulling force results in unbinding in the PC1 direction with negligible motion along PC2.

Next, we measured the force-dependent bond lifetimes of WT-Ecad in 2.5 mM $Ca^{2+}$. Because WT-Ecads can unbind/rebind in ~1 s (20) as the proteins shuttle between X-dimer and S-dimer, we allowed the WT-Ecads to interact for both long (3.0 s) and short (0.3 s) periods of time (Fig. 5 *D* and *E*). In both cases, the WT-Ecads formed bonds that had a weak dependence on pulling force, likely due to dissociation of the intermediate conformation. Our previous AFM force-clamp data (22) that showed that WT-Ecads form weak force-dependent bonds even when the time of contact is reduced to 1 ms suggest that the transition from X-dimer to the intermediate state occurs rapidly. Although we had previously interpreted the weak force-dependent bonds at short contact times to be ideal bonds, our current experiments, performed with more stringent data selection criteria, suggest that these bonds may possess some slip-bond properties. It is also possible that the difference compared with ref. 22 arises from the transient nature of the intermediate state from which cadherins unbind. (20). The intrinsic parameters for K14E and WT cadherin dimers (Table S3) were obtained by fitting the data to a microscopic slip-bond model (44, 45).

Finally, we engineered a weaker-affinity W2F-Ecad conformational shuttling mutant by replacing Trp2 with Phe2 (*Methods*). Our single-molecule measurements with the W2F-Ecad showed that these constructs formed very-short-lifetime ideal bonds that remain insensitive to pulling force at both short (0.3 s) and long (3.0 s) contact times (Fig. 5 *F* and *G*), suggesting that the W2F-Ecad remain in an intermediate conformation at both interaction times. This result is consistent with a recent report that W2F mutants form an equilibrium ensemble of X-dimers and S-dimers (21). When we globally fit the measured force vs. lifetime data to the slip-bond model described above, the distance between the bound state and the transition state ($x_\beta$) along the pulling coordinate was zero (Table S4), indicating that the pathway for the unbinding of the W2F mutant was independent of force.

## Discussion

Our study integrates computer simulations and single-molecule force measurements to predict the energy landscape for cadherin adhesion and the transition pathway for interconversion between X-dimers and S-dimers and to identify cadherin structures that form ideal bonds. We show that ideal bonds are formed due to the force-induced dissociation of an intermediate conformation in the X-dimer to S-dimer interconversion pathway. Pulling on this intermediate state causes a torsional motion perpendicular to the applied force. Cadherin unbinding along a pathway orthogonal to the pulling coordinate results in identical molecular extensions in the bound and transition states, resulting in force-independent ideal bonds. Our study demonstrates that a simple one-dimensional energy landscape, which assumes conformational motions along the pulling direction, fails to capture the rich dynamics of cadherin response to mechanical force. Multidimensional energy landscapes have previously been reported for the refolding of RNA hairpins and pulling of DNA toward denatured structures (46, 47).

Both WT-Ecad and W2F mutants adopt an intermediate state resembling an X-dimer, albeit with swapped N-terminal β-strands. Because the pair of K14–D138 salt bridges are not present in the intermediate state, its unbinding motion along the pulling direction and orthogonal to the pulling coordinate is less constrained. In addition, a Pro5–Pro6 motif that is buried in the adhesive interface prevents opposing protomers from forming a tight contact (37) and enables the EC1 domains to twist past each other as the pulling force unbinds the proteins. Our AFM force-clamp measurements confirm that unbinding of the intermediate state results in ideal bond formation. Although a similar torsional motion is also observed in the W2A mutants, the K14–D138 salt-bridge pair that is present in this mutant locks the proteins together and results in catch bonds due to force-induced hydrogen bond formation (23). However, torsional motion weakens the pulling force dependence of the W2A catch bonds; consequently, these catch bonds have very short peak lifetimes that range between 0.06 s to 0.1 s (22, 23).

Force-free solution binding measurements report that S-dimers have a ~10-fold higher binding affinity than X-dimers (12, 48). Our approximate energy landscapes also support this conclusion (Fig. 1*A*). However, our data also indicate that the energetic differences between X-dimers and S-dimers are insufficient to preclude them from interconverting. In fact, two complementary approaches—the coarse-grained knowledge-based energy landscapes as well as MD based on all atomic force-fields—yield structural intermediates between the X-dimer and S-dimer forms that are highly similar. The MD trajectories are also clearly seen to carefully avoid the central high-energy region of the PC1–PC2 space, thus validating our predicted energy landscape. The shuttling between X-dimer and S-dimer conformations likely explains why the WT and W2F Ecads do not form slip bonds that are a signature of the S-dimer conformation.

Because key structural features of *trans* dimers formed by both the truncated ectodomains (used in our simulations) and by the complete ectodomain are very similar, the force-induced multidimensional unbinding that we observe will likely be seen using full-length cadherin ectodomains. In particular, the angle between opposing EC1 domains in the WT-Ecad *trans* dimer crystal structure used in our simulations (85°) is similar to the angle (91°) in full-length Ecad *trans* dimers (PDB ID code 3Q2V) (49), suggesting that our results are not an artifact of using just the outer two EC domains in the simulations. Similarly, because the EC1–EC1 angle (78°) in the Ncad WT EC1-EC2 *trans* dimer structure (PDB ID code 2QVI) is similar to the EC1–EC2 WT-Ecad *trans* dimer crystal structure, it is likely that the results obtained with the W2F Ncad crystal structure apply to W2F Ecads as well.

In intercellular junctions, cadherins self-organize to form a 2D lattice where proteins from opposing cells form *trans* dimers whereas proteins on the same cell surface participate in lateral *cis* interactions (49). Within this 2D lattice, the *trans* dimers orient their unique *cis* interface in nearly perpendicular directions (49). The orthogonal orientation of opposing *trans*- and *cis*- binding interfaces limit force-induced torsional motion orthogonal to the pulling direction (Fig. S3). Consequently, our data suggest that only stand-alone *trans* dimers, which are not incorporated in *cis* clusters, form ideal bonds. Because ideal bonds have low lifetimes and are preferentially ruptured by mechanical force, they may serve to enhance the fraction of *cis* clusters on the cell surface.

## Methods

**PCA.** Eleven crystal structures (3LNE, 1EDH, 1FF5, 1Q1P, 2QVF, 3LNG, 3LNH, 3LNI, 3Q2L, 3Q2N, and 3Q2V) of classical cadherins were obtained from the PDB. After processing the files to remove all hetero atoms, the structures were aligned to the structure 3LNE by use of the Procrustes analysis algorithm implemented in MATLAB. Based on this structural alignment, a set of 411 residues present in all of the structures was retained for further analysis. The aligned 3D position coordinates (x, y, and z) of the $C^\alpha$ atoms in each structure constitute a multivariate dataset for PCA, $\Xi_{n\times p}$ where the number of structures $n = 11$ and the number of variables $p = 3N$, where $N = 411$, the

number of residues considered in each structure. The variance–covariance matrix $\boldsymbol{S}$ of the dataset is obtained as

$$s_{ij} = E\left[\left(\xi_i - \bar{\xi}_i\right)\left(\xi_j - \bar{\xi}_j\right)\right] \;\forall\; 1 \le i, j \le 3N, \quad [1]$$

where $\xi_k$ refers to the $k^{th}$ variable (x, y, or z coordinate) and $\bar{\xi}_k$ refers to the mean of the $k^{th}$ variable. The covariance matrix $\boldsymbol{S}$ is decomposed as $\boldsymbol{S} = \boldsymbol{E}\Delta\boldsymbol{E}^T$, where the columns of $\boldsymbol{E}$ are the eigenvectors arranged in the decreasing order of the eigenvalues (elements of the diagonal matrix $\Delta$). The amount of variance captured by each eigenvector is obtained from its eigenvalue. The projections of the points on each eigenvector $\boldsymbol{PC}_{n\times 3N} = \boldsymbol{\Xi}_{n\times 3N} \times \boldsymbol{E}_{3N\times 3N}$ are called the PCs. The projections of the mean centered data onto the PCs are called the PC scores, $\boldsymbol{P}_{n\times 3N} = \left(\boldsymbol{\xi} - \left(\vec{1}_{p\times 1} \times \bar{\boldsymbol{\xi}}^T\right)\right) \times \boldsymbol{E}_{3N\times 3N}$, where $\bar{\boldsymbol{\xi}}^T$ is the transpose of the mean vector of position coordinates.

**Projecting Energy Landscapes onto PC Coordinates.** Representative structures were sampled uniformly at equally spaced points along the first and second eigenvectors from the PCA to produce a rectangular grid. The limits of the grid were obtained from the range of PC scores observed among the 11 crystal structures. The coordinates of each representative structure on the grid were calculated using the coordinates of a central structure $R_0$ (closest to the origin) on the PC grid and the PC eigenvectors. The 3D coordinates $\boldsymbol{R}_{1\times 3N}$ of a structure $R$ on the PC grid at position $(R_1, R_2)$ could be obtained from the position coordinates of $R^0$ as

$$\boldsymbol{R}_{1\times 3N} = \boldsymbol{R}^0_{1\times 3N} + \left(R_1 - R_1^0\right) \times \boldsymbol{e}_1 + \left(R_2 - R_2^0\right) \times \boldsymbol{e}_2, \quad [2]$$

where $(R_1^0, R_2^0)$ were the scores of $R^0$ along $PC1$ and $PC2$ and $\boldsymbol{e}_1$ and $\boldsymbol{e}_2$ were the eigenvectors corresponding to the first and second PCs. The potential energy of each structure was estimated as an optimized linear combination of three different knowledge-based potential terms that we previously developed: four-body sequential potential, four-body nonsequential potential, and short-range potentials (50–53). The potential energy was calculated as

$$V_{opt} = V_{4-body\ seq} + 0.28 * V_{4-body\ non-seq} + 0.22 * V_{short\ range}. \quad [3]$$

Here, the term "four-body" refers to spatially close groups of four amino acids that can interact. Details on how the weights for the different terms were obtained (35) by minimizing the RMSD of best decoys from homology modeling targets of CASP8 (54) to their corresponding native structures using particle swarm optimization (55) have been described previously.

**Determination of Transition Path Between X-Dimers and Stand-Swap Dimers.** Conformational changes between large molecules such as cadherins can be efficiently captured using coarse-grained models such as ENMs (56–58). To generate a transition path between two forms, we used the PATH-ENM server (36). The method combines the ENM potentials of the two end-point structures into a smoothly interpolated mixed potential function with one saddle point (corresponding to the transition state) and two minima (corresponding to start and end conformations). The transition path between the start and end conformations was obtained as the lowest-energy path that connects these structures via the saddle point. The structural intermediates along this transition path were projected onto the PC1–PC2 space obtained from the 11 crystal structures. Only the $C^{\alpha}$ atoms of residues were used in the model and the distance cutoff for interresidue interactions was chosen as 1.3 nm.

**MD and SMD Simulations and Structural Analysis.** MD and SMD simulations were performed using the Condo cluster at the High Performance Computing facility at Iowa State University. Four cadherin crystal structures were used in all of the MD and SMD simulations. Of these, the K14E mutant (PDB ID code 3LNE), WT (PDB ID code 2QVF), and W2A mutant (PDB ID code 3LNH) structures were from Ecad and the W2F mutant (PDB ID code 4NUQ) structure was from Ncad. S-dimers were built from the crystallographic structure of their EC1–EC2 chains by applying crystallographic symmetry operations. Before simulations were performed, missing amino acid residues were added using Swiss-PDBViewer v4.1. All simulations were performed using GROMACS 4.6.5 software with GROMOS 53a6 force field and SPC216 water model.

The MD and SMD simulations were carried out similarly to the method reported in our previous paper (23). Briefly, for MD simulations, the cadherin dimer crystal structures were positioned at the center of a triclinic box that was scaled by the protein dimensions; the box was sized so that no protein atom was closer than 1 nm from the walls of the box. The solvated box sizes were $11 \times 9 \times 7$ nm$^3$ (W2A), $15 \times 9 \times 7$ nm$^3$ (W2F), $15 \times 9 \times 7$ nm$^3$ (WT), and $16 \times 7 \times 7$ nm$^3$ (K14E). The solvated box contains 66,877 atoms, 83,446 atoms, 85,144 atoms, and 75,193 atoms, respectively, for W2A, W2F, WT, and K14E dimer structure MD simulations. The solvated box systems were charge-neutralized with the appropriate number of $Na^+$ ions. Steric clashes within the box were eliminated by minimizing the potential energy of the system. Before a production MD run, we first equilibrated the water molecules and ions by establishing and maintaining a 300-K temperature using a modified Berendsen thermostat and stabilizing the pressure at 1 atm under isothermal–isobaric conditions using a Parinello–Rahman barostat. Once equilibration was attained, MD runs were performed for 150 ns with a 2-fs integration step using LINCS constraints and with frames recorded at 2-ps intervals. A 1-nm cutoff was used both for van der Waals interactions and for electrostatic interactions using the particle mesh Ewald technique. Periodic boundary conditions were assumed in all simulations. To monitor the evolution of structures in the MD simulations, we calculated RMSDs by least-square fitting each trajectory to either its starting structure or to the X-dimer crystal structure.

Three structures—one taken at the end of the MD simulation at 150 ns, another at 140 ns, and a third at 100 ns—from each of the four MD simulations were used as starting conformations for the corresponding SMD simulations. The SMD starting structures of WT, W2F, and W2A dimers were placed at the center of 12- × 40- × 8-nm$^3$ triclinic boxes, whereas the K14E mutant was embedded at the center of a 40- × 12- × 8-nm$^3$ box, with the longest dimension along the applied force direction. Each system consisted of ∼122,455 atoms (K14E mutant), ∼146,815 atoms (WT), ∼136,417 atoms (W2F mutant), and ∼136,466 atoms (W2A mutant). All SMD simulations used an umbrella pulling method using a harmonic spring with stiffness k = 332 pN/nm. Similar to our AFM force measurements where the biotinylated C-terminal end of a complete EC1–EC5 cadherin repeat is pulled, this virtual harmonic spring pulled the opposing protomers apart at a constant velocity of 0.4 nm/ns. The C-terminal residue of one protein chain was designated as the pulling group and the C-terminal residue from the other chain was the reference group. All SMD simulations are integrated at every 2-fs step with LINCS constraints and frames are recorded every 1 ps (Figs. S4–S6). To determine how the proteins dissociate in the SMD simulations, the vectors of the long helical axis of opposing EC1 domains was determined every 1 ps using VMD 1.9.1. Using these vectors, two sets of angles were computed using MATLAB: the angles between the EC1 domains at each time point (angular separation) and the EC1–EC1 angles along PC2 (torsion angle). The minimum/maximum torsion angles were determined by taking the average of 100 data points around the minimum and maximum values. The difference between the minimum and maximum values were recorded as peak-to-peak torsion angles.

**Ecad Constructs and Single-Molecule Force-Clamp Measurements.** To engineer W2F mutants, the full EC region of Ecad with a C-terminal Avi tag was cloned into pcDNA3.1(+) vectors using primers containing a Tev sequence and His tag. This resulted in an ORF of the complete Ecad/Avi/Tev/His sequence. The W2F mutation was introduced in the EC1 domain of Ecad/ATH by point mutation using QuikChange kit (Agilent). The engineered cadherin sequence was transfected into HEK 293 cells, which was selected using 400 μg/mL of Geneticin (G418; Invitrogen). Cells were grown to confluency in high-glucose DMEM containing 10% (vol/vol) FBS and 200 μg/mL G418 and then exchanged into serum-free DMEM. Conditioned media was collected 4 d after media exchange. Purification and biotinylation of the W2F mutant, WT-Ecad, and the K14E mutant followed protocols described previously (22). Briefly, the cadherin EC constructs were purified using a Nickel-NTA resin (Invitrogen) and biotinylated at the C-terminal Avi tag site using BirA enzyme (BirA500 kit; Avidity).

Before the single-molecule force-clamp spectroscopy experiments, glass coverslips and $Si_3N_4$ AFM cantilevers were cleaned and functionalized with biotinylated cadherin monomers. The protocol used for cadherin immobilization has been previously described (22, 23). Briefly, the cantilevers and coverslips were functionalized with amine groups using a 2% vol/vol solution of 3-aminopropyltriethoxysilane (Sigma) in acetone. The amine groups were subsequently decorated with polyethylene glycol spacers (PEG 5000; Laysan Bio) containing an amine-reactive *N*-hydroxysuccinimide ester on one end; 7% of the PEGs were functionalized with a biotin group at the other end. Before affixing cadherins on functionalized surfaces, the coverslips and cantilevers were incubated overnight in a 0.1 mg/mL BSA solution to minimize nonspecific binding. Following BSA incubation, the functionalized coverslips and cantilevers were incubated with 0.1 mg/mL streptavidin. Biotinylated cadherin monomers (150–200 nM for 45 min) were then bound to the immobilized streptavidin. Free biotin binding sites of streptavidin molecules were blocked by 0.02 mg/mL solution of biotin.

Single-molecule force-clamp spectroscopy experiments were performed using an Agilent 5500 AFM with a closed-loop piezoelectric scanner. Force measurements were carried out in a 10 mM Tris,100 mM NaCl, and 10 mM KCl, pH 7.5, buffer solution containing either 2.5 mM $CaCl_2$ (WT-Ecad and W2F-Ecad) or 1.5 mM $CaCl_2$ (K14E-Ecad). The cadherin-functionalized AFM tip and glass coverslip were brought into contact for 0.3 s or 3.0 s. The tip

was then withdrawn from the substrate at a rate of 100–600 pN/s and clamped at a constant force. Lifetimes were determined from the persistence time of the bond at each clamping force. To unambiguously identify specific unbinding events from nonspecific and multiple unbinding, the force-clamp events were converted to force vs. tip-surface distance traces. Unbinding distance obtained in every trace was compared with the theoretical value determined using an extended freely jointed chain model (59) for PEG.

**ACKNOWLEDGMENTS.** This work was supported in part by a American Cancer Society Research Scholar Grant 124986-RSG-13-185-01-CSM (to S.S.) and National Science Foundation (NSF) Grant MCB-1021785 (to R.L.J.). Simulations were supported in part by the research information technology team at Iowa State University, utilizing HPC@ISU equipment, some of which has been purchased through funding provided by NSF MRI Grant CNS 1229081 and CRI Grant 1205413.

1. Gumbiner BM (2005) Regulation of cadherin-mediated adhesion in morphogenesis. *Nat Rev Mol Cell Biol* 6(8):622–634.
2. Halbleib JM, Nelson WJ (2006) Cadherins in development: Cell adhesion, sorting, and tissue morphogenesis. *Genes Dev* 20(23):3199–3214.
3. Niessen CM, Leckband D, Yap AS (2011) Tissue organization by cadherin adhesion molecules: Dynamic molecular and cellular mechanisms of morphogenetic regulation. *Physiol Rev* 91(2):691–731.
4. Harris TJ, Tepass U (2010) Adherens junctions: From molecules to morphogenesis. *Nat Rev Mol Cell Biol* 11(7):502–514.
5. Brasch J, Harrison OJ, Honig B, Shapiro L (2012) Thinking outside the cell: How cadherins drive adhesion. *Trends Cell Biol* 22(6):299–310.
6. Pokutta S, Weis WI (2007) Structure and mechanism of cadherins and catenins in cell-cell contacts. *Annu Rev Cell Dev Biol* 23:237–261.
7. Shapiro L, Weis WI (2009) Structure and biochemistry of cadherins and catenins. *Cold Spring Harb Perspect Biol* 1(3):a003053.
8. Leckband D, Sivasankar S (2012) Cadherin recognition and adhesion. *Curr Opin Cell Biol* 24(5):620–627.
9. Leckband D, Sivasankar S (2012) Biophysics of cadherin adhesion. *Subcell Biochem* 60:63–88.
10. Shapiro L, et al. (1995) Structural basis of cell-cell adhesion by cadherins. *Nature* 374(6520):327–337.
11. Nagar B, Overduin M, Ikura M, Rini JM (1996) Structural basis of calcium-induced E-cadherin rigidification and dimerization. *Nature* 380(6572):360–364.
12. Harrison OJ, et al. (2010) Two-step adhesive binding by classical cadherins. *Nat Struct Mol Biol* 17(3):348–357.
13. Boggon TJ, et al. (2002) C-cadherin ectodomain structure and implications for cell adhesion mechanisms. *Science* 296(5571):1308–1313.
14. Pertz O, et al. (1999) A new crystal structure, Ca2+ dependence and mutational analysis reveal molecular details of E-cadherin homoassociation. *EMBO J* 18(7):1738–1747.
15. Ciatto C, et al. (2010) T-cadherin structures reveal a novel adhesive binding mechanism. *Nat Struct Mol Biol* 17(3):339–347.
16. Sivasankar S, Zhang Y, Nelson WJ, Chu S (2009) Characterizing the initial encounter complex in cadherin adhesion. *Structure* 17(8):1075–1081.
17. Häussinger D, et al. (2004) Proteolytic E-cadherin activation followed by solution NMR and X-ray crystallography. *EMBO J* 23(8):1699–1708.
18. Parisini E, Higgins JM, Liu JH, Brenner MB, Wang JH (2007) The crystal structure of human E-cadherin domains 1 and 2, and comparison with other cadherins in the context of adhesion mechanism. *J Mol Biol* 373(2):401–411.
19. Hong S, Troyanovsky RB, Troyanovsky SM (2011) Cadherin exits the junction by switching its adhesive bond. *J Cell Biol* 192(6):1073–1083.
20. Li Y, et al. (2013) Mechanism of E-cadherin dimerization probed by NMR relaxation dispersion. *Proc Natl Acad Sci USA* 110(41):16462–16467.
21. Vendome J, et al. (2014) Structural and energetic determinants of adhesive binding specificity in type I cadherins. *Proc Natl Acad Sci USA* 111(40):E4175–E4184.
22. Rakshit S, Zhang Y, Manibog K, Shafraz O, Sivasankar S (2012) Ideal, catch, and slip bonds in cadherin adhesion. *Proc Natl Acad Sci USA* 109(46):18815–18820.
23. Manibog K, Li H, Rakshit S, Sivasankar S (2014) Resolving the molecular mechanism of cadherin catch bond formation. *Nat Commun* 5:3941.
24. Teodoro ML, Phillips GN, Jr, Kavraki LE (2003) Understanding protein flexibility through dimensionality reduction. *J Comput Biol* 10(3-4):617–634.
25. Teodoro ML, Phillips GN, Jr, Kavraki LE (2002) A dimensionality reduction approach to modeling protein flexibility. *Proceedings of the Sixth Annual International Conference on Computational Biology* (Assoc for Computing Machinery, New York), pp 299–308.
26. Yang L, Song G, Carriquiry A, Jernigan RL (2008) Close correspondence between the motions from principal component analysis of multiple HIV-1 protease structures and elastic network modes. *Structure* 16(2):321–330.
27. Yang LW, Eyal E, Bahar I, Kitao A (2009) Principal component analysis of native ensembles of biomolecular structures (PCA_NEST): Insights into functional dynamics. *Bioinformatics* 25(5):606–614.
28. Hub JS, de Groot BL (2009) Detection of functional modes in protein dynamics. *PLOS Comput Biol* 5(8):e1000480.
29. Maisuradze GG, Liwo A, Scheraga HA (2009) Principal component analysis for protein folding dynamics. *J Mol Biol* 385(1):312–329.
30. Haliloglu T, Bahar I (2015) Adaptability of protein structures to enable functional interactions and evolutionary implications. *Curr Opin Struct Biol* 35:17–23.
31. Sankar K, Liu J, Wang Y, Jernigan RL (2015) Distributions of experimental protein structures on coarse-grained free energy landscapes. *J Chem Phys* 143(24):243153.
32. Zhang Y, Arakaki AK, Skolnick J (2005) TASSER: An automated method for the prediction of protein tertiary structures in CASP6. *Proteins* 61(Suppl 7):91–98.
33. Bradley P, et al. (2005) Free modeling with Rosetta in CASP6. *Proteins* 61(Suppl 7): 128–134.
34. Skolnick J (2006) In quest of an empirical potential for protein structure prediction. *Curr Opin Struct Biol* 16(2):166–171.
35. Gniewek P, Leelananda SP, Kolinski A, Jernigan RL, Kloczkowski A (2011) Multibody coarse-grained potentials for native structure recognition and quality assessment of protein models. *Proteins* 79(6):1923–1929.
36. Zheng W, Brooks BR, Hummer G (2007) Protein conformational transitions explored by mixed elastic network models. *Proteins* 69(1):43–57.
37. Vendome J, et al. (2011) Molecular design principles underlying β-strand swapping in the adhesive dimerization of cadherins. *Nat Struct Mol Biol* 18(6):693–700.
38. Oostenbrink C, Villa A, Mark AE, van Gunsteren WF (2004) A biomolecular force field based on the free enthalpy of hydration and solvation: The GROMOS force-field parameter sets 53A5 and 53A6. *J Comput Chem* 25(13):1656–1676.
39. Van Der Spoel D, et al. (2005) GROMACS: Fast, flexible, and free. *J Comput Chem* 26(16):1701–1718.
40. Cailliez F, Lavery R (2006) Dynamics and stability of E-cadherin dimers. *Biophys J* 91(11):3964–3971.
41. Bayas MV, Schulten K, Leckband D (2004) Forced dissociation of the strand dimer interface between C-cadherin ectodomains. *Mech Chem Biosyst* 1(2):101–111.
42. Zhang Y, Sivasankar S, Nelson WJ, Chu S (2009) Resolving cadherin interactions and binding cooperativity at the single-molecule level. *Proc Natl Acad Sci USA* 106(1):109–114.
43. Efron B (1982) *The Jackknife, the Bootstrap, and Other Resampling Plans* (Society for Industrial and Applied Mathematics, Philadelphia).
44. Dudko OK, Hummer G, Szabo A (2006) Intrinsic rates and activation free energies from single-molecule pulling experiments. *Phys Rev Lett* 96(10):108101.
45. Dudko OK, Hummer G, Szabo A (2008) Theory, analysis, and interpretation of single-molecule force spectroscopy experiments. *Proc Natl Acad Sci USA* 105(41):15755–15760.
46. Hyeon C, Thirumalai D (2007) Measuring the energy landscape roughness and the transition state location of biomolecules using single molecule mechanical unfolding experiments. *J Phys Condens Matter* 19:113101.
47. Gore J, et al. (2006) DNA overwinds when stretched. *Nature* 442(7104):836–839.
48. Katsamba P, et al. (2009) Linking molecular affinity and cellular specificity in cadherin-mediated adhesion. *Proc Natl Acad Sci USA* 106(28):11594–11599.
49. Harrison OJ, et al. (2011) The extracellular architecture of adherens junctions revealed by crystal structures of type I cadherins. *Structure* 19(2):244–256.
50. Feng Y, Kloczkowski A, Jernigan RL (2007) Four-body contact potentials derived from two protein datasets to discriminate native structures from decoys. *Proteins* 68(1):57–66.
51. Feng Y, Kloczkowski A, Jernigan RL (2010) Potentials 'R' Us web-server for protein energy estimations with coarse-grained knowledge-based potentials. *BMC Bioinformatics* 11:92.
52. Bahar I, Kaplan M, Jernigan RL (1997) Short-range conformational energies, secondary structure propensities, and recognition of correct sequence-structure matches. *Proteins* 29(3):292–308.
53. Zimmermann MT, Leelananda SP, Kloczkowski A, Jernigan RL (2012) Combining statistical potentials with dynamics-based entropies improves selection from protein decoys and docking poses. *J Phys Chem B* 116(23):6725–6731.
54. Cozzetto D, et al. (2009) Evaluation of template-based models in CASP8 with standard measures. *Proteins* 77(Suppl 9):18–28.
55. Kennedy J, Eberhart R (1995) Particle swarm optimization. *Proceedings of the IEEE International Conference on Neural Networks* (IEEE, New York), pp 1942–1948.
56. Tirion MM (1996) Large amplitude elastic motions in proteins from a single-parameter, atomic analysis. *Phys Rev Lett* 77(9):1905–1908.
57. Bahar I, Atilgan AR, Erman B (1997) Direct evaluation of thermal fluctuations in proteins using a single-parameter harmonic potential. *Fold Des* 2(3):173–181.
58. Atilgan AR, et al. (2001) Anisotropy of fluctuation dynamics of proteins with an elastic network model. *Biophys J* 80(1):505–515.
59. Oesterhelt F, Rief M, Gaub HE (1999) Single molecule force spectroscopy by AFM indicates helical structure of poly(ethylene-glycol) in water. *New J Phys* 1:6.1–6.11.